Force cycles and force chains

Antoinette Tordesillas,* David M. Walker, and Qun Lin
Department of Mathematics and Statistics, University of Melbourne, Parkville, Victoria 3010 Australia
(Received 29 June 2009; revised manuscript received 14 October 2009; published 13 January 2010)

We examine the coevolution of N cycles and force chains as part of a broader study which is designed to quantitatively characterize the role of the laterally supporting contact network to the evolution of force chains. Here, we elucidate the rheological function of these coexisting structures, especially in the lead up to failure. In analogy to force chains, we introduce the concept of force cycles: N cycles whose contacts each bear above average force. We examine their evolution around force chains in a discrete element simulation of a dense granular material under quasistatic biaxial loading. Three-force cycles are shown to be stabilizing structures that inhibit relative particle rotations and provide strong lateral support to force chains. These exhibit distinct behavior from other cycles. Their population decreases rapidly during the initial stages of the strain-hardening regime—a trend that is suddenly interrupted and reversed upon commencement of force chain buckling prior to peak shear stress. Results suggest that the three-force cycles are called upon for reinforcements to ward off failure via shear banding. Ultimately though, the resistance to buckling proves futile; buckling wins under the combined effects of dilatation and increasing compressive load. The sudden increase in three-force cycles may thus be viewed as an indicator of imminent failure via shear bands.

DOI: 10.1103/PhysRevE.81.011302 PACS number(s): 45.70.−n

I. INTRODUCTION

Fruit vendors through history have understood the benefits of a packing rich in 3 cycles: a favored arrangement in many fruit packings in which three objects are arranged in mutual contact. Supporting elements arranged in 3 cycles (e.g., trusses) also form the basic "building blocks" of countless structures, bridges, towers, and machines. Indeed, the ubiquity of such elements in everyday life is a testament to the strength and stability of the triangle as a structural shape. For this reason, columns and other major structural supports are often reinforced by these stabilizing agents. To what extent are these structural motifs found in granular materials? Do these materials, known for their propensity to self-organize, construct internal structures that exhibit these features? In this paper, we explore the functionality and evolution of such mesoscopic structures in a quasistatically deforming granular material. Attention is paid to the coexistence and hence the integrated evolution of these structures with the phenomenon of "force chains."

Force chains have attracted widespread interest (e.g., [1–11] and references therein) owing to their primary role in force transmission and energy dissipation. These quasilinear structures bear and transmit the compressive load on the system, the effectiveness of which depends on the lateral support provided by their confining neighbors [1,2,12]. A detailed characterization of these laterally supporting contacts is thus necessary for the knowledge of not only force transmission but also stability of dense granular systems. To date, very little is known about the nature of this support [12]. A way forward is to examine the contact topology of this support and its strain evolution within the framework of graph theory—specifically, from the standpoint of *N cycles*. An N cycle in an undirected graph is a closed path or a noninteracting walk of length N, where $N \geq 3$ with no repeated vertices other than its initial and final vertex [13]. In this context, force chains exist conjoined with cycles. (In graph theory, a cycle is sometimes called a circuit. However, cycles or circuits bear a different meaning to "loops:" a loop is defined to be an edge joining a vertex to itself.) In contrast to force chains, cycles have received scant attention, especially in regard to their evolution in a deforming medium [14]; see also [8,9,15,16] for earlier studies of these structures in static and deforming granular packings. To the best of our knowledge, the coevolution of cycles and force chains has not yet been investigated. Three cycles, dominant in dense granular systems, suppress rotations [15,16]. Thus, the question which lends particular interest to the coexistence of these structures is the extent to which the relatively unstable force chains depend on 3 cycles for support. The techniques of graph theory and the cognate area of complex networks offer a relatively nascent yet promising approach to this problem [10,11,14–16]. This study could have far-reaching implications. Understanding the evolution of force chains and their stability is a fundamental goal of granular physics; it is also central to constitutive theory which aims to deliver robust predictions of granular behavior in a diverse range of processes, e.g., in geology, physics, and civil and chemical engineering [1,2,5,10,11,14]. Further afield, this study may beneficially impact (i) other areas of materials science, as analogous force networks exist in various soft condensed matter [17–19], and (ii) other areas of complex science where networks inhabit similar motifs, e.g., chemical, biological, and telecommunication structures [20], particularly as motifs in granular networks lend themselves to direct physical analysis and interpretation.

Numerous studies of two-dimensional systems using particle data from discrete element method (DEM) simulations and experiments on photoelastic disk assemblies have shown that force chains generally align in the direction of maximum compressive principal stress [1,2,5–7,21]. Thus, under continued loading and loss of lateral support due to dilatation,

*Corresponding author; atordesi@ms.unimelb.edu.au

these axially compressed particle columns become unstable and prone to buckling [1,2,12]. There is mounting evidence that force chain failure via buckling, a mechanism governed by large relative rotations, is the underpinning mechanism for shear bands (e.g., [1,2,6,7,21]).

A recent study of the stability and buckling of force chains from DEM and photoelastic disk experiments confirmed that relative rotations between particles form the primary contact motion in confined force chain buckling [6,12,21,22]. Mechanisms that provide resistance to this motion (e.g., sliding and rolling friction), both within the force chain as well as in the contacts with and within the laterally supporting neighbors, would therefore serve to stabilize force chains. Results from DEM simulations also suggest that the stability of these laterally supporting contacts bears a major influence on the load-carrying capacity of force chains [12,22]. Evidence from structural mechanics analysis corroborates this and further suggests that the duration of elastic-plastic bucking is longest if the contact failure nucleates from force chain contacts (i.e., between force chain particles): that is, the laterally supporting contacts remain stable and elastic as the limiting rolling resistance at force chain contacts is reached [12,23,24]. These structural stability studies have also shown quantitatively the governing influence of the laterally supporting contacts on the critical buckling load and corresponding buckling modes of force chains, both in the absence and presence of geometrical imperfections (i.e., misalignment). However, as in any structural mechanics analysis, these formulations require information on the spatial distribution and forces imparted by the lateral supporting contacts. Currently, the modeler is faced with the difficult challenge of making a judicious choice from a vast number of possible configurations to achieve progress in the analysis [12,23,24]—this points to a glaring gap in the knowledge on force chains. Consequently, studies aimed at unraveling the nature of these supports and their *integrated evolution with force chains* are warranted. In this paper, we report on a detailed analysis of the coevolution of contact cycles and force chains using data from a DEM simulation of a densely packed cohesionless granular assembly under biaxial loading [6].

The remainder of this paper is organized as follows. In Sec. II we briefly describe the DEM model, loading conditions, and parameters used. As force chains are one of the most fundamental structures in a deforming granular material we present in Sec. III a summary of the algorithms used to identify force chains and their failure via confined buckling. Section IV introduces our concept of force cycles and investigates the interplay between these structures and force chains. We shed light on the spatial distribution and strain evolution of three-force cycles and their dual function with respect to force chain evolution and shear band development in Sec. V. The paper is closed in Sec. VI with a synopsis.

II. DISCRETE ELEMENT MODEL

The DEM model consists of a densely packed polydisperse assembly of spherical particles constrained to move along a plane throughout the loading history [6,7]. This DEM model has been employed to examine the constitutive response of other granular assemblies subject to a variety of compression and penetration tests (e.g., [6,7,12,21,22]). Resistances to relative motion at the particle-particle and particle-wall contacts are governed by combinations of a linear spring, a dashpot, and a friction slider. The model is designed to mimic the response of assemblies of noncircular particles (e.g., [25]). Thus, it incorporates a moment transfer to account for rolling resistance in accordance with [26,27]. This modification to the classical DEM model of Cundall and Strack [28], which allows the relative rotations of particles at contacts to be controlled, has been found to be essential in achieving more realistic rotations and stress predictions (e.g., [29–33]).

A combination of Hooke's and Coulomb's laws defines the interaction between contacting particles, namely,

$$\mathbf{f}^n = k^n \Delta \mathbf{u}^n + b^n \Delta \mathbf{v}^n, \tag{1}$$

$$\mathbf{f}^t = \begin{cases} k^t \Delta \mathbf{u}^t + b^t \Delta \mathbf{v}^t & \text{for} |\Delta \mathbf{u}^t| < \mu |\mathbf{f}^n| / k^t \\ \mu |\mathbf{f}^n| & \text{for} |\Delta \mathbf{u}^t| \geq \mu |\mathbf{f}^n| / k^t, \end{cases} \tag{2}$$

where $\mathbf{f}^n$ and $\mathbf{f}^t$ are the normal and tangential components of the contact force, k^n and k^t are spring stiffness coefficients, b^n and b^t are the viscous damping coefficients, and μ is the Coulomb friction coefficient. Following the modified DEM in [26,27], the rolling resistance or contact moment—defined in an analogous fashion to Coulomb's law—is expressed as

$$\mathbf{I}^c = \begin{cases} k^r \Delta \alpha + b^r \Delta \dot{\alpha} & \text{for} |\Delta \alpha| < \mu^r R_{min} |\mathbf{f}^n| / k^r \\ \mu^r R_{min} |\mathbf{f}^n| & \text{for} |\Delta \alpha| \geq \mu^r R_{min} |\mathbf{f}^n| / k^r, \end{cases} \tag{3}$$

where R_{min} denotes the smaller of the radii of the two interacting particles, k^r is the spring stiffness coefficient, and μ^r is the friction coefficient. The remaining quantities in the above relations are the relative normal and tangential displacements and relative rotations denoted, respectively, by $\Delta \mathbf{u}^n$, $\Delta \mathbf{u}^t$, and $\Delta \alpha$; $\Delta \mathbf{v}^n$, $\Delta \mathbf{v}^t$, and $\Delta \dot{\alpha}$ represent the relative normal and tangential translational and rotational velocities, respectively.

Table I provides a summary of the simulation and material parameters used. The particular assembly comprises 5098 circular particles, created randomly, the radii of which are uniformly distributed between $[\frac{2}{3}R, \frac{4}{3}R]$ where $R = 1.14$ mm. The initial configuration is isotropic with a solid fraction of 0.858, a value slightly above the jamming transition where the system first attains mechanical equilibrium. The vertical walls are frictionless so that particles can slide and roll along them without any resistance; otherwise, all other material properties are identical to those of the particles. The top and bottom walls are assumed to have the same material properties as the particles. The stiffness coefficient for the rolling resistance is chosen based on the assumption that, under equilibrium conditions, contact moments due to rolling resistance are comparable to the moments due to the tangential forces [6].

The initial sample is prepared by dropping particles into the (rectangular) container under a gravitational field with the friction coefficient between particles set to zero. The assembly is left to settle until the kinetic energy is negligible. The sample is compressed at a constant strain rate in the

TABLE I. DEM parameters and material properties used.

Parameter	Value
Applied strain rate $\dot{\varepsilon}_{yy}$	-8×10^{-3}/s
Confining pressure σ_{xx}	7.035×10^{2} N/m
Time-step increment	4×10^{-6} s
Initial height:width ratio	1:1
Number of particles	5098
Particle density	2.65×10^{3} kg/m^3
Smallest radius	$\frac{2}{3}R$
Largest radius	$\frac{4}{3}R$
Average radius R	1.14×10^{-3} m
Initial packing density	0.858
Interparticle friction μ	0.7
Particle-wall friction μ (top, bottom)	0.7
Particle-wall friction μ (sides)	0.0
Rolling friction μ^r	0.02
Normal spring stiffness k^n	1.05×10^{5} N/m
Tangential spring stiffness k^t	5.25×10^{4} N/m
Rotational spring stiffness k^r	6.835×10^{-2} N m/rad

vertical direction, while allowed to expand in the horizontal direction under a constant confining pressure. The rate of compression is given by $\dot{\varepsilon}_{yy}=-0.008$ s^{-1}. Inertial effects are quantified by the dimensionless group $\dot{\varepsilon}_{yy}\sqrt{m_{av}/\sigma_{xx}}$, where m_{av} is the average particle mass and σ_{xx} is the confining pressure. This dimensionless group is on the order of 10^{-5}, which is significantly less than that suggested to correspond to the transition between the quasistatic and dense flow regimes of 10^{-3} [34]. Damping coefficients are assigned values according to the formulas $b^n=0.1\sqrt{m_{min}k^n}$, $b^t=0.1\sqrt{m_{min}k^t}$, and $b^r=0.1R_{min}\sqrt{m_{min}k^r}$, where m_{min} is the mass of the smaller particle. Additional simulations performed at even smaller rates of deformation confirmed that the strain rate is sufficiently small to ensure quasistatic conditions. The discrete time step used in the numerical integration of the equations of motion is assigned a value according to $\Delta t=0.1\sqrt{m_{min}k^n}=4\times10^{-6}$ s. Additional tests with smaller time steps have been performed: no effect on the particle dynamics has been observed. The average overlap between particles depends on the value of the stiffness coefficient k^n and the assumed confining pressure σ_{xx}. The ratio $\sigma_{xx}/k^n=0.0067$, which results in an average overlap between particles of approximately 1%, was chosen so that strain localization and, in particular, the formation of a persistent shear band are reproduced.

The strain evolution of the system exhibits distinct regimes of deformation, typically seen for dense cohesionless granular assemblies (e.g., dry sand under plane strain biaxial compression [35]): a period of strain-hardening regime, followed by strain softening and, finally, the so-called critical state regime. The strain hardening is characterized by a monotonic increase with axial strain of the shear stress to a peak value, with the applied shear stress being given by the stress ratio $(\sigma_{xx}-\sigma_{yy})/(\sigma_{xx}+\sigma_{yy})$. Postpeak, relatively large fluctuations are evident: the ensuing strain-softening regime is characterized by a sequence of precipitous drops in the shear stress before the critical state regime where the shear stress then fluctuates about an essentially steady-state value (we show this later along with other system properties). A single persistent shear band governs the dynamics in the critical state regime. The sample dilates globally prior to this regime. The onset of global dilation occurs in the latter half of the strain-hardening regime, with the maximum rate achieved just after the peak shear stress during the strain-softening regime. Global dilation of the sample essentially ceases during the critical state, although small fluctuations about the near constant bulk volume are evident. These small fluctuations are due to particle rearrangements inside the shear band [6,21,22]. Inside the band, two concurrent mechanisms prevail: collapse by buckling of old force chains and birth of new force chains. These mechanisms lead to dilatant and contractant particle rearrangements within the shear band, and their relative dominance ultimately governs the fluctuations seen on the global scale (e.g., [21]).

III. FORCE CHAINS

To examine the evolution of force chains, we employ the quantitative method for identifying force chains and their failure by confined buckling in [6,7,36]. Here, a force chain is considered to be a *physical structure* comprising a quasilinear chain of particles. We now summarize the essential features of these algorithms for completeness. Particles in force chains can be identified using their particle load vectors. This vector, computed for each particle, is derived from the tensor $\hat{\sigma}_{ij}$, which is expressed as follows:

$$\hat{\sigma}_{ij}=\sum_{c=1}^{\alpha} f_i^c r_j^c, \tag{4}$$

where α is the number of contacting neighbors of the particle, and f_i^c and r_j^c denote the components of the contact force and the unit normal vector from the center of the particle to the point of contact. The largest eigenvalue of this tensor and its corresponding eigenvector define, respectively, the magnitude and direction of the particle load vector. A chain of three or more particles whose particle load vectors align within a prescribed small tolerance angle and whose particle load magnitudes each exceeds the global average value is defined as a force chain. Note that this global average value varies with strain in a qualitatively similar manner to that of the shear stress: in particular, it reaches a peak value at the same strain state as the peak shear stress. An example force chain from the sample at a strain state just after the peak shear stress is shown in Figs. 1(a) and 1(b).

When a structure buckles from axial compression, the axial load it carries decreases as its constituent elements displace laterally. Accordingly, in order to identify force chains that have buckled over a given strain interval $[\varepsilon^A,\varepsilon^B]$, the following three-step process of elimination is applied. First, all particles that are not in force chains at ε^A are eliminated. This leaves only force chains to be analyzed. Thus, in the second step, a force chain whose member particles do not individually sustain a drop in the magnitude of their particle

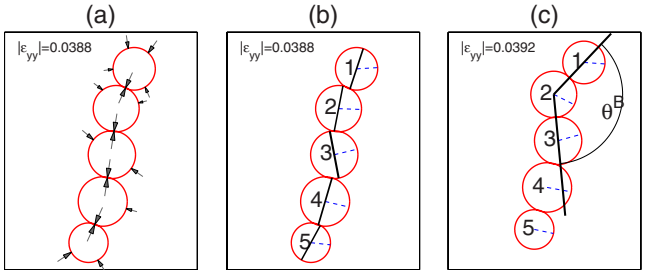

FIG. 1. (Color online) (a) Contact forces on a force chain in black arrows and (b) corresponding particle load vectors whose direction and magnitude are indicated by the alignment and thickness of the (black) solid lines. (c) The force chain buckles during $[\varepsilon^A, \varepsilon^B]=[0.0388, 0.0392]$, for a buckling threshold of $\theta^*=1°$; the angle θ^B is shown for segment 1-2-3. The change in the orientation of the (blue) dashed line from center to edge of particles in (b) and (c) indicates rotations.

load vector during $[\varepsilon^A, \varepsilon^B]$ is eliminated. Out of the remaining force chains, all contiguous three-particle segments within each chain are analyzed in the third and final steps. In the example force chain shown in Figs. 1(b) and 1(c), there are three such segments, i.e., particles 1-2-3, 2-3-4, and 3-4-5, to be analyzed over the strain interval $[\varepsilon^A, \varepsilon^B]=[0.0388, 0.0392]$. Specifically, the change in the alignment of each such segment in a force chain is computed via the buckling angle θ, which is given by $\theta=(\theta^A-\theta^B)/2$, where θ^A and θ^B are the subtended angles of the outer particles with respect to the central particle in the segment at strain states ε^A and ε^B, respectively, and $0<\theta^B<\theta^A\leq\pi$. A force chain segment, as well as the force chain it is part of, is deemed to have buckled if the buckling angle exceeds a prescribed threshold θ^*, i.e., $\theta^*<\theta$. The sensitivity of the above procedures to the thresholds used in these algorithms has been studied extensively elsewhere using data from both DEM simulations and photoelastic disk experiments [6,7,12,21,22,36]; a global average particle load vector magnitude for the force chain algorithm along with $\theta^*=1°$ for the buckling algorithm is a physically reasonable choice.

IV. FORCE CYCLES AND FORCE CHAINS

We construct a network or graph to examine the connectivity of the entire assembly and its evolution. A vertex of the contact network represents an individual particle, and an edge between two vertices exists if the corresponding particles are in direct physical contact. Note that this abstraction is solely focused on the *connectivity* of the physical system—defined by the contacts between particles. The resulting network is undirected and unweighted. Moreover, it is important to keep in mind that deformation which is governed by the relative motion of the constituent particles may or may not lead to changes in the contact network. Any change in the network depends exclusively on the generation of new and/or loss of existing contacts. We have studied the evolving properties of such a contact network as the material deforms elsewhere [37]. Here, we focus on the as yet unexplored minimal cycle bases of the graph at each strain state

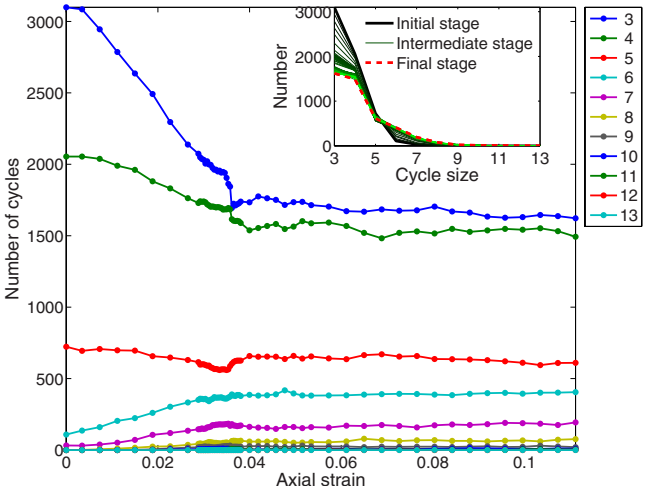

FIG. 2. (Color online) Evolution of the population of minimal cycles C_N with respect to axial strain. Lines with dots in order of upper to lower represent cycles C_3 through C_{13}. Inset shows corresponding frequency distribution. Peak shear stress for this sample occurs at axial strain $|\varepsilon_{yy}|=0.034$ [6]. Initial stage is indicated by thick black solid line, final stage is indicated by (red) dashed line, and intermediate stages go from dark to light (green) as strain increases.

and their evolving properties throughout the different stages of loading—particularly in the lead up to failure. A minimal cycle basis of a graph is a set containing the shortest cycles, i.e., cycles with minimum length or number of edges. In what follows, we investigate how a minimal cycle basis of the contact network evolves with increasing axial strain and study the crucial interplay between such cycles and force chains. There are a number of established algorithms for obtaining a minimal cycle basis for a complex network. We used the algorithm of Horton [38] in conjunction with a faster variant due to Mehlhorn and Michail [39]. In general, the minimal cycle bases are nonunique. However, this issue which may be particularly important in nonplanar graphs does not affect the distribution of cycle sizes (e.g., [40]), which is the focus of this study.

Odd cycles are structures in which relative rotations are "frustrated" and thereby act as stabilizing agents, while even cycles allow rolling without slipping and are more akin to roller bearings [15,16]. We identify these structures in our assembly by first computing the population of the various minimal cycles in the sample and tracking their evolution with axial strain. Figure 2 shows the populations of cycles classified according to size or order N, i.e., the number of vertices in the cycle. Low-order cycles, namely, 3 and 4 cycles, dominate the contact topology. Here, 3 cycles (uppermost curve) form the clear majority throughout loading history and show the greatest rate of degradation as the system dilates in the approach to peak shear stress and global failure. The population of 5 cycles (third curve from the top) remains essentially invariant, whereas higher-order cycles, i.e., C_N (with $N>5$) gradually increase in numbers in the strain-hardening regime due to dilatation. The total population of each cycle class remains essentially invariant in the critical state regime. The transition of low- to higher-order cycles

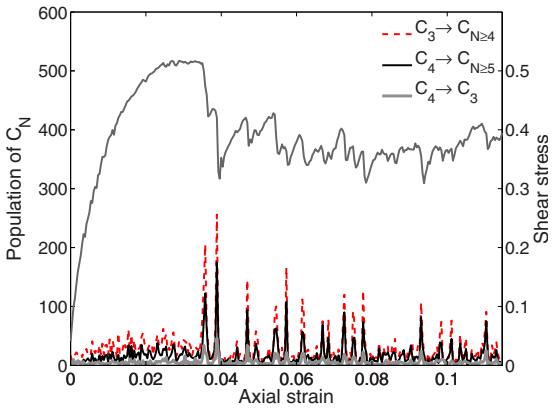

FIG. 3. (Color online) Transition of low-order cycle populations to higher-order cycles. A large rise in the number of 3 cycles (dashed red line) and 4 cycles (solid black line) becoming higher-order cycles due to dilatation correlates with drops in shear stress. Conversely, the number of 4 cycles collapsing to 3 cycles (solid gray line) is much less.

because of dilatation can be seen more clearly in Figs. 3 and 4. Over axial strain intervals that correspond to drops in shear stress, the number of 3 cycles which open up to become part of higher-order cycles dramatically increases (Fig. 3). A similar trend is seen for 4 cycles which cleave and join others to form higher-order cycles. In contrast, the population of 4 cycles collapsing to 3 cycles is far less. An example of the evolution of the dominant 3/4 cycles to higher-order cycles is shown in Fig. 4. While the growth of higher-order cycles are associated with dilatation, we emphasize here that

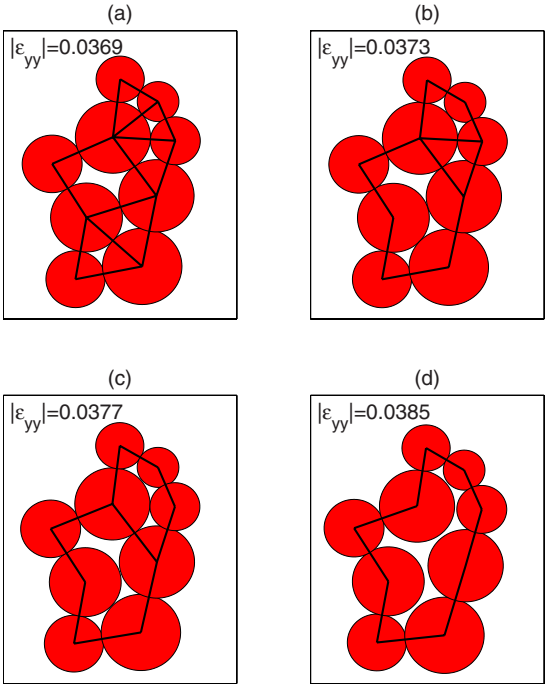

FIG. 4. (Color online) An example cycle evolution in a particle cluster taken from the sample. (a) 3 and 4 cycles in a particle cluster. These open up and combine to form (b) 6 cycles in the lower left portion of the particle cluster and (c) 5 cycles in the upper right portion of the cluster, ultimately leading to (d) single 9 cycles.

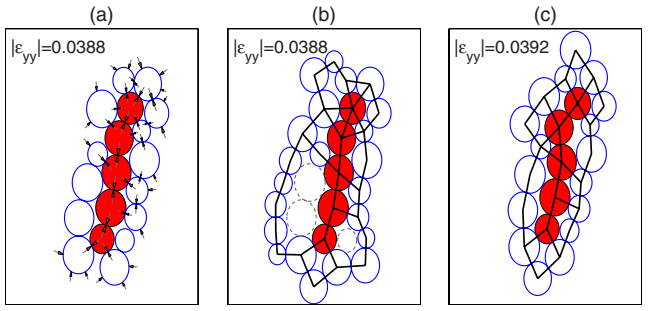

FIG. 5. (Color online) (a) The unbuckled force chain (red solid particles) shown in Fig. 1(a) and its confining neighbors (blue outlined particles). (b) Distribution of cycles around this force chain; rattlers which bear only one contact, particles delineated in dashed outline in the figure, are excluded in a minimal cycle basis. (c) Buckled force chain configuration, as in Fig. 1(c), with confining neighbors and cycle membership.

the size of each cycle provides only a partial indication of the actual void area encapsulated within that cycle of contacts. Recall that the graph from which these cycles are determined solely depends on connectivity; no other aspect of the physical system (e.g., particle sizes) is incorporated in this analysis.

At any given strain state, a force chain will be part of contact cycles C_N of various sizes N as exemplified in Fig. 5. In this context, force chains are distinct from cycles in that force chains are physical structures made up of particles, whereas cycles are made up of contacts. We first consider the ratio of the most dominant C_N to the total number of cycles for each force chain and then average these for all force chains. As shown in Fig. 6(a), the fraction of 4 cycles around force chains is essentially constant compared to that for the 3 cycles, which decreases rapidly until the strain corresponding to the peak shear stress is reached, before leveling off in

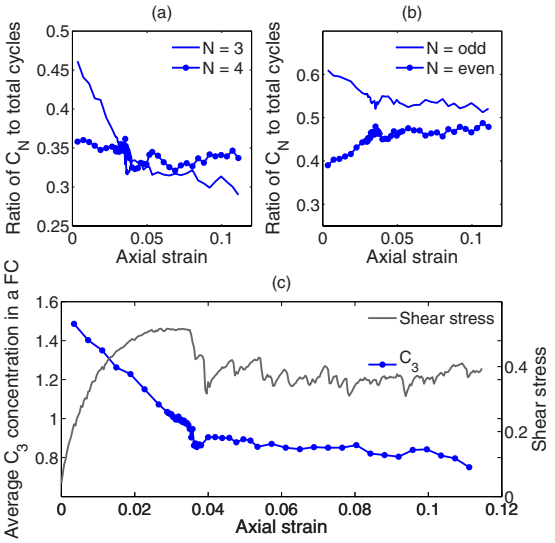

FIG. 6. (Color online) (a),(b) Strain evolution of the average ratio of the number of C_N to the total number of cycles around force chains. (c) shows strain evolution of the average concentration of 3 cycles in a force chain together with shear stress.

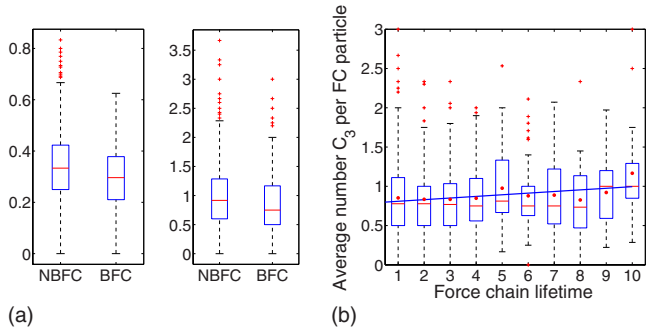

FIG. 7. (Color online) (a) Left: ratio of 3 cycles to all cycles during force chain lifetime classified by nonbuckling (NBFC) and buckling (BFC). Right: concentration of 3 cycles in a force chain (NBFC and BFC). (b) Box plot of average ratio of number of 3 cycles per force chain particle over force chain lifetime during shear band development. Red lines inside the boxes show the median of the data, dots are the mean, and blue line is a straight line fit to the mean. Red crosses represent outliers [41].

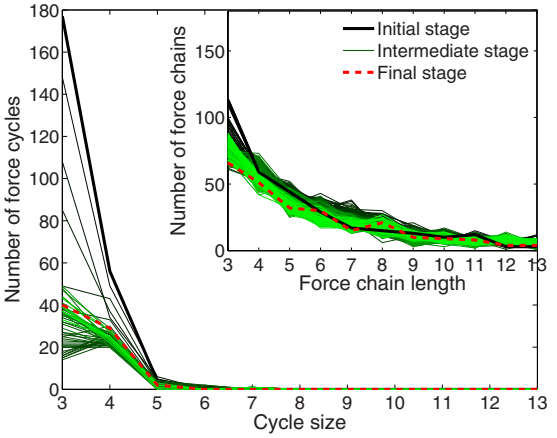

FIG. 8. (Color online) Frequency distribution of force cycles C_N^f for various strain states through to critical state. Inset shows corresponding distribution of force chains (schemes are as inset of Fig. 2).

the critical state regime. The same trend can be observed inside the shear band, although the fluctuations there are slightly larger. Qualitatively, the average fraction of odd cycles to the total number of cycles in a force chain is the same as that seen for 3 cycles; conversely, the average fraction of even cycles increases around force chains during the strain-hardening regime [Fig. 6(b)]. The concentration of 3 cycles in a force chain, computed as the ratio of the number of 3 cycles to the total number of particles in a force chain, is shown in Fig. 6(c): as the material reacts to continued loading, the major load-carrying force chains are losing the stabilizing benefits of 3 cycles. One may then ask if 3 cycles really do promote the stability of force chains.

We classify force chains into two categories: those which do not fail by buckling [nonbuckling force chain (NBFC)] and those which do [buckling force chain (BFC)] using the algorithm outlined in Sec. III, and we consider if the concentration of 3 cycles is higher for nonbuckling than for buckling force chains throughout a chains' lifetime. The box plots [41] of Fig. 7(a) show that (left panel) NBFCs have a higher number of 3 cycles compared to higher-order cycles than BFCs and (right panel) the concentration of 3 cycles in a NBFC is higher than in a BFC [42]. It is apparent then that force chains with a higher concentration of 3 cycles are more stable. We can exemplify this further by showing in Fig. 7(b) the strain evolution of the average number of 3 cycles per force chain particle with respect to a force chain's lifetime during the development of the shear band; here, a force chain lifetime is the strain interval over which the particle chain is classified as a force chain, as defined earlier in Sec. III. Note that during the development of the shear band, most force chains (97%) have a lifetime of ten increments of strain or less. A straight line fit to the mean lifetime of these chains (Pearson's correlation coefficient of 0.60) clearly shows (positive coefficient) that force chains with a higher concentration of 3 cycles survive longer.

To explore the role of these stabilizing cycles further, we now introduce the concept of a "force cycle" C_N^f. Analogous to force chains in which each particle load vector magnitude is above the global average, a force cycle is a cycle whose contacts *each* carry above the global average of the contact force magnitudes. Note that this cycle classification is decided purely on the basis of force magnitude and not direction. Keep in mind that each of these force thresholds varies with axial strain and qualitatively exhibits the same evolution as seen for the shear stress: monotonic increase to a peak value at the same strain state as the peak shear stress, then a short period of decrease with strain, before leveling off to a near steady-state value in the critical state regime.

As shown in Figs. 8 and 9, there is a distinct difference in the evolution of the distribution of force cycles to the general cycle membership in Fig. 2: low-order force cycles decrease and then increase before saturating in the critical state. This change is greatest in the three-force cycles which undergo a

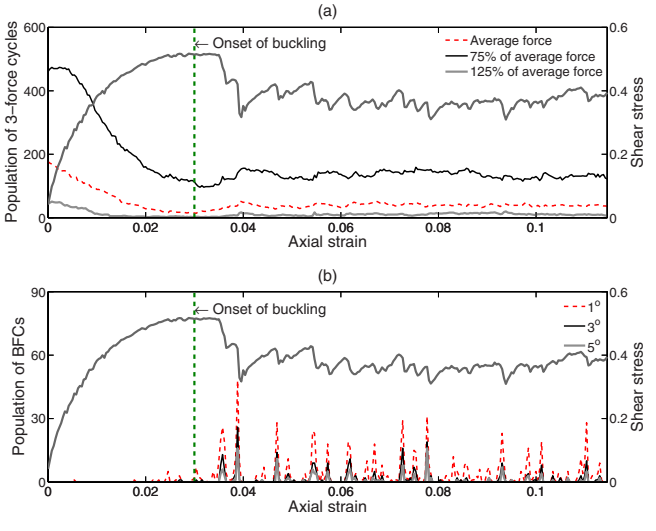

FIG. 9. (Color online) (a) Strain evolution of the population of three-force cycles together with the shear stress. (b) Strain evolution of the population of buckling force chains at three different threshold buckling angles together with the shear stress. Vertical green dashed line indicates the onset of buckling force chains detected away from the boundaries.

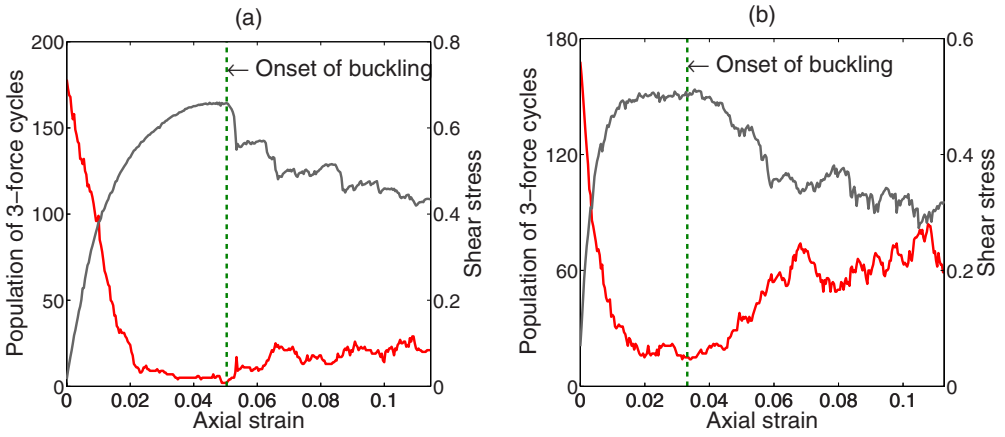

FIG. 10. (Color online) Strain evolution of the population of three-force cycles together with the shear stress for two systems identical in every respect to that considered in Fig. 9 except for the following aspects: (a) the rolling resistance is higher, i.e., rolling friction $\mu^r = 0.2$ [22]; (b) the loading condition is strain-controlled biaxial compression under constant volume [21]. Vertical green dashed line indicates onset of buckling force chains detected away from the boundaries.

drop in population to as low as 8% of its initial value. The evolution in the population distribution of force chains is by comparison subtle, with the greatest drop in the population seen for three-force chains and a fall to as low as 54% of its initial value.

Figure 9(a) shows that the rapid decrease in the population of three-force cycles is interrupted at the strain when the first force chain buckling occurs (around $|\varepsilon_{yy}|=0.030$) or when the shear band nucleates. At this point (vertical dashed line), the trend suddenly reverses and new three-force cycles emerge. The growth of three-force cycles continues until the shear band is fully developed (around $|\varepsilon_{yy}|=0.038$) and the critical state commences. We observed no such decisive trend in higher-order force cycles nor in the evolution of either the total population of force chains or force chains of length 3.

We tested the extent to which these findings are robust to differences in the three main aspects of this study: (i) thresholds used to detect these structures, (ii) material properties, and (iii) loading conditions. Akin to force chains, the definition of a force cycle depends on a threshold value, namely, the global average contact force magnitude. In Fig. 9(a) we show by plotting the population of three-force cycles for thresholds of 25% above and below this global average value that the same general trends are observed. That is, there is a drop in the number of three-force cycles followed by an increase at the onset of buckling toward small fluctuations around a steady value postpeak shear stress in the critical state regime. Therefore, analogous to thresholds in the force chain algorithm there is some robustness across a wide range of values and selecting the threshold to be the average global value appears to be a reasonable choice. Similarly, the population of buckling force chains is shown in Fig. 9(b) for various threshold buckling angles to demonstrate the period of commencement of buckling. We note that in this and other tests undertaken, there are strain states in the early stages of loading in which the buckling algorithm detects a few force chains buckling next to the boundaries [note the small peaks prior to green dashed line in Fig. 9(b)]; however, these events do not appear to trigger the persistent shear band. The green dashed vertical line in Fig. 9(a) marks the first strain state where a buckling force chain is detected within the sample away from the boundaries. This onset of buckling has been examined in detail in earlier studies using other measures such as local nonaffine measures of micropolar deformation, energy dissipation, volumetric strain rate, and particle rotation (e.g., [6,21,22]). In all these studies, the shear band nucleates just before the peak shear stress with buckling force chains detected in the middle of the sample.

Notice the correlation between the low- to high-order cycle transitions in Fig. 3 and the sudden bursts in the population of buckling events in Fig. 9(b). This feature is consistent with earlier findings from experiment and DEM simulation which show that *confined buckling of force chains* not only induces dilatant rearrangements among its surrounding particles—it is also an inherently dilatant mesoscopic mechanism, as is evident in the growth of encapsulated void and cycle size in the top right portion of the buckled force chain segment 1-2-3 in Fig. 5(c) (e.g., [21,22]).

We observed the trends uncovered above for the samples examined in earlier studies [6,12,21,22]: these not only included assemblies of different material properties [see, for example, Fig. 10(a)], but also different biaxial loading conditions [see, for example, Fig. 10(b)]. Compared to the sample considered in Fig. 9, the material in Fig. 10(a) is more resistant to interparticle rolling due to its higher rolling resistance; note that by interparticle rolling, we mean those contacts whose contact moment $\mathbf{I}^c$ is at the plastic threshold, as defined in Eq. (3) [6]. The higher rolling friction clearly bolsters the material's ability to resist and thus delay the onset of failure. This is evident in the higher peak shear stress and corresponding strain state in Fig. 10(a) versus those seen in Fig. 9: similarly, force chain buckling, shear banding, and sudden growth of three-force cycles all initiate at a higher strain than that in the weaker material in Fig. 9.

V. DUAL ROLE OF FORCE CYCLES

What then is the purpose of these newly born three-force cycles? Do these strong cycles emerge to serve as reinforce-

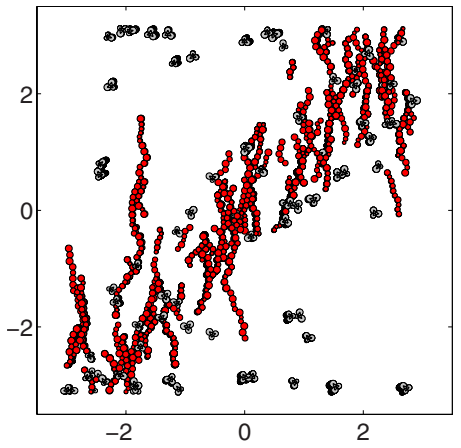

FIG. 11. (Color online) Spatial distribution of three-force cycles (gray) together with force chains that have buckled (red) during the development of shear band.

ments to force chains during the onset of global instability? We found that 98% of the three-force cycles that emerge during shear band development are part of force chains and 77% of 3 cycles share this property. Furthermore Fig. 11 shows that these three-force cycles are mainly concentrated in the shear band: the region where instability initiates. Thus, the escalation of three-force cycles essentially occurs at the onset of buckling, emerging in the location where force chain buckling concentrates (Figs. 9–11). Since earlier results suggest that three-force cycles enhance stability of force chains (92% are in NBFCs), the material appears to be rearranging itself to counter this loss of stability at both the time and locale of greatest need.

As three-force cycles are strong 3 cycles, they provide a dual resistance to buckling: (i) by resisting relative rotations and (ii) by providing strong lateral support and effectively propping up force chains as they buckle. We found that relative rotations in three-force cycles are generally lower, as shown in Fig. 12. In this figure, the relative incremental rotations of all the contacts in the region of the shear band and during all strain stages of its development (i.e., $0.030 \leq |\varepsilon_{yy}| \leq 0.038$) are first computed. The relative incremental rotation, measured in radians, is the relative value of the contacting particles' rotations over a single time step in the simulation. The shear band in this system is approximately inclined at 45° anticlockwise to the positive x axis, with the central axis of the band extending from the lower left to the upper right corner of the specimen [6]. We thus approximated the region where the shear band develops to be a straight band whose boundaries lie parallel to and within ten particle diameters from the central axis of the shear band. The thickness of this band region is determined from the particle rotations averaged over all particles at fixed distances from this central axis: a plot of the distribution of these averaged particle rotations is shown in [6]: it exhibits an essentially even symmetry with the rotation increasing from zero at the band boundaries to a maximum in the middle of the band. Similarly, a relatively large gradient in the velocity profile can also be observed along these band boundaries [6]. These kinematical patterns are consistent

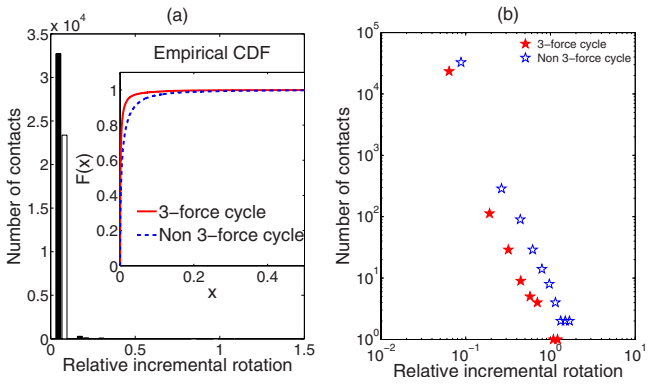

FIG. 12. (Color online) (a) Histograms of relative particle rotations at contacts in three-force cycles (black bar) and all other contacts (white bar) within and during the development of the shear band. Rotations are measured in radians. Inset: the empirical cumulative distribution functions. (b) Equivalent to (a) but plotted on a log-log scale. Contacts within three-force cycles clearly exhibit lower relative particle rotations (frustrated) than other contacts. This is confirmed by a Kolmogorov-Smirnov test whose null hypothesis of samples that are drawn from the same distribution can be rejected at the 5% level of significance.

with those deemed to be the best indicators of shear band boundaries in earlier studies [26,27]. All the contacts in the shear band region are then classified into two groups: those belonging to three-force cycles and those that do not. The empirical distributions of the relative incremental rotations for each group are shown in Fig. 12. A Kolmogorov-Smirnov test shows these distributions to be distinct clearly demonstrating that three-force cycle contacts exhibit lower relative incremental rotations than other contacts, i.e., frustrated rotations.

Figure 13(a) illustrates the dual resistance to force chain buckling imparted by three-force cycles. We further determined the two most prevalent stabilizing conformations in which three-force cycles emerge: 80% are arranged as configuration A providing strong lateral support, whereas 20% are arranged as configuration B so helping to prop up buckling force chains [Fig. 13(b)]. However, the presence of

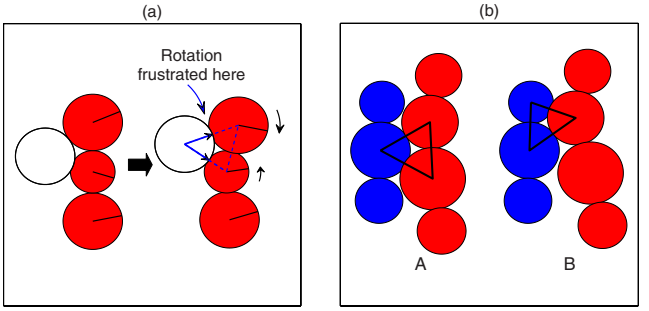

FIG. 13. (Color online) (a) Three-force cycles provide a dual resistance to force chain buckling: by impeding rotation which tend to dominate during buckling and by providing strong lateral support with above global average forces propping up the force chain. (b) Prevalent supporting three-force-cycle configurations of force chains. Red particles (light) form a force chain; blue particles (dark) may or may not form another force chain.

three-force cycles does not always prevent instability: 14% are present in buckling force chains (6% are in both NBFC and BFC). The increase in three-force cycles during shear band development appears therefore to be a last ditch attempt of the material to stabilize the system. However, due to the continued loading of the sample under dilatation, the effectiveness of these reinforcements is only momentary. In the end, buckling "wins." We might therefore regard the appearance of these three-force cycles to be a signature of impending failure. In comparison to three-force cycles, an increase in the number of four-force cycles is only seen after peak shear stress ratio, i.e., once the shear band has effectively fully developed.

VI. SUMMARY

In summary, we have examined the role of local contact topology around columnar particle structures known as force chains in the context of evolving contact network cycles C_N. A study of the evolution of C_N in the lead up to force chain buckling, and thus shear banding, reveals that three-force cycles are a key source of stability—effectively called upon as reinforcements at commencement of force chain buckling or the onset of shear banding. We have shown that newly born three-force cycles emerge during shear band development and are spatially concentrated in shear bands, often existing as part of a force chain. Three-force cycles thus act to secure and reinforce force chain columns creating a competition between the combined effect of increased loading and dilatation of the assembly and the material's attempts to support the load and maintain stability. This attempt to resist buckling in the form of three-force cycles, however, ultimately proves futile. Force chain buckling wins resulting in the full development of the shear band. This study has brought to the fore the relevance of N cycles in a complex network, in particular three cycles, in the development of precursory failure events such as force chain buckling and shear banding for dense granular systems. We have taken steps in a number of fronts including the quantitative characterization of lateral contacts around force chains and uncovered some of the underlying structural design principles of self-organization in dense granular materials under shear, using techniques from graph theory. As trusses proliferate civil engineering structures to enhance stability, this paper has highlighted that a deforming granular material also tries to arrange itself into analogous mutually supportive structures to prevent failure. We hope that insights gained from studies of this kind can be one day harnessed in the design and synthesis of discrete materials with tailor made properties.

ACKNOWLEDGMENTS

This study was supported by the U.S. Army Research Office (Grant No. DAAD W911NF-07-1-0370) and the Australian Research Council (Grants No. DP0558808 and No. DP0772409). We thank Dr. J. Shi for insightful discussions. We thank the anonymous referees for constructive comments on an earlier version of this manuscript.

[1] M. Oda and H. Kazama, Geotechnique **48**, 465 (1998).
[2] M. Oda, J. Konishi, and S. Nemat-Nasser, Mech. Mater. **1**, 269 (1982).
[3] F. Radjai, D. E. Wolf, M. Jean, and J. J. Moreau, Phys. Rev. Lett. **80**, 61 (1998).
[4] F. Radjai, M. Jean, J. J. Moreau, and S. Roux, Phys. Rev. Lett. **77**, 274 (1996).
[5] T. S. Majmudar and R. P. Behringer, Nature (London) **435**, 1079 (2005).
[6] A. Tordesillas, Philos. Mag. **87**, 4987 (2007).
[7] M. Muthuswamy and A. Tordesillas, J. Stat. Mech.: Theory Exp. 2006, P09003.
[8] R. Blumenfeld, Phys. Rev. Lett. **93**, 108301 (2004).
[9] P. T. Metzger, Phys. Rev. E **70**, 051303 (2004).
[10] A. A. Peña, S. McNamara, P. G. Lind, and H. J. Herrmann, Granular Matter **11**, 243 (2009).
[11] A. A. Peña, H. J. Herrmann, and P. G. Lind, in *Powders and Grains*, Sixth International Conference on Micromechanics of Granular Media, edited by M. Nakagawa and S. Luding (AIP, Melville, NY, 2009), pp. 321–324.
[12] A. Tordesillas and M. Muthuswamy, J. Mech. Phys. Solids **57**, 706 (2009).
[13] B. Bollobás, *Modern Graph Theory* (Springer, New York, 2008).
[14] A. G. Smart and J. M. Ottino, Phys. Rev. E **77**, 041307 (2008).
[15] N. Rivier, in *Powders and Grains*, Fifth International Conference on Micromechanics of Granular Media, Stuttgart Vol. 1, edited by R. García-Rojo, H. J. Herrmann, and S. McNamara (A. A. Balkema, The Netherlands, 2005), pp. 29–32.
[16] H. J. Herrmann, in *Trends in Computational Structural Mechanics*, edited by W. A. Wall, K.-U. Bletzinger, and K. Schweizerhof (CIMNE, Barcelona, 2001).
[17] A. Tanguy, J. P. Wittmer, F. Leonforte, and J.-L. Barrat, Phys. Rev. B **66**, 174205 (2002).
[18] N. Lacevic and S. C. Glotzer, J. Phys. Chem. B **108**, 19623 (2004).
[19] J. Zhou, S. Long, Q. Wang, and A. D. Dinsmore, Science **312**, 1631 (2006).
[20] S. Boccaletti, V. Latora, Y. Moreno, M. Chavez, and D.-U. Hwang, Phys. Rep. **424**, 175 (2006).
[21] A. Tordesillas, J. Zhang, and R. Behringer, Geomech. Geoeng. **4**, 3 (2009).
[22] A. Tordesillas and M. Muthuswamy, Acta Geotechnica **3**, 225 (2008).
[23] A. Tordesillas and J. Shi, Int. J. Numer. Analyt. Meth. Geomech. **33**, 1737 (2009).
[24] G. Hunt, A. Tordesillas, S. Green, and J. Shi, Philos. Trans. R. Soc. London, Ser. A **368**, 249 (2010)
[25] N. Estrada, A. Taboada, and F. Radjai, Phys. Rev. E **78**, 021301 (2008).

[26] K. Iwashita and M. Oda, Powder Technol. **109**, 192 (2000).
[27] M. Oda and K. Iwashita, Int. J. Eng. Sci. **38**, 1713 (2000).
[28] P. A. Cundall and O. D. L. Strack, Geotechnique **29**, 47 (1979).
[29] F. Alonso-Marroquin, S. Luding, H. J. Herrmann, and I. Vardoulakis, Phys. Rev. E **71**, 051304 (2005).
[30] H. Sakaguchi, E. Ozaki, and T. Igarashi, Int. J. Mod. Phys. B **7**, 1949 (1993).
[31] N. Hu and J. F. Molinari, J. Mech. Phys. Solids **52**, 499 (2004).
[32] M. J. Jiang, H. S. Yu, and D. Harris, Comput. Geotech. **32**, 340 (2005).
[33] S. Ji, D. M. Hanes, and H. H. Shen, Mech. Mater. **41**, 764 (2009).
[34] F. da Cruz, S. Emam, M. Prochnow, J.-N. Roux, and F. Chevoir, Phys. Rev. E **72**, 021309 (2005).
[35] A. L. Rechenmacher, J. Mech. Phys. Solids **54**, 22 (2006).
[36] J. F. Peters, M. Muthuswamy, J. Wibowo, and A. Tordesillas, Phys. Rev. E **72**, 041307 (2005).
[37] D. M. Walker and A. Tordesillas, Int. J. Solids Struct. Int. J. Solids Struct., 624 (2010).
[38] J. D. Horton, SIAM J. Comput. **16**, 358 (1987).
[39] K. Mehlhorn and D. Michail, ACM J. Exp. Algorithmics 11, article no. 2.5 (2006) http://doi.acm.org/10.1145/1187436.1216582.
[40] P. M. Gleiss, P. F. Stadler, A. Wagner, and D. A. Fell, Adv. Complex Syst. **4**, 207 (2001).
[41] Box plots are a concise way of summarizing distributions by representing the 25th, 50th (median), and 75th percentiles by a box with whiskers covering a wide range of the data (e.g., 99.3%) under an assumption of a normal distribution. Data points outside this range (outliers) can be plotted individually. [See, for example, box plot in MATLAB (The MathWorks, Natick, MA).]
[42] A Wilcoxon rank sum test in both cases confirms that this difference in the medians is statistically significant.